Ecosystem Health and Sustainability
A SCIENCE PARTNER JOURNAL

RESEARCH ARTICLE

Extreme Precipitation and High-Temperature Impacts on Terrestrial Gross Primary Productivity across China, 1981 to 2100

Zichong Su[1†], Huizhu Yang[2†], Youjia Liang[1,2,3*], Lijun Liu[4], Jia Sun[3,5], and Liangcun Jiang[1]

[1]School of Resources and Environmental Engineering, Wuhan University of Technology, Wuhan 430070, China. [2]South China Institute of Environmental Sciences, Ministry of Ecology and Environment and The Key Laboratory of Urban Ecological Environment Simulation and Protection, Ministry of Ecology and Environment of the People's Republic of China, Guangzhou 510535, China. [3]Key Laboratory of Remote Sensing Application and Innovation, Chongqing 401147, China. [4]School of Information Engineering, Wuhan Business University, Wuhan 430056, China. [5]Chongqing Meteorological Service, Chongqing 401147, China.

*Address correspondence to: yjliang@whut.edu.cn
†These authors contributed equally to this work.

Citation: Su Z, Yang H, Liang Y, Liu L, Sun J, Jiang L. Extreme Precipitation and High-Temperature Impacts on Terrestrial Gross Primary Productivity across China, 1981 to 2100. *Ecosyst. Health Sustain.* 2025;11:Article 0462. https://doi.org/10.34133/ehs.0462

Submitted 30 June 2025
Revised 10 November 2025
Accepted 2 December 2025
Published 15 December 2025

The interplay of extreme precipitation and high temperature markedly diminishes the carbon sink capacity of China's terrestrial ecosystems. Although the spatiotemporal evolution characteristics of these extreme events have been initially identified, their impacts on gross primary production (GPP) remain inadequately quantified. With the multisource data (1981 to 2100) of 4 shared socioeconomic pathways (SSPs), the Mann–Kendall test, empirical orthogonal function, and center of gravity shift models were used to identify the spatiotemporal evolution of GPP, and the structural equation model was used to elucidate the pathways and contributions of extreme events to GPP changes. GPP increased nationwide (0.02 to 0.07 kg C m^{-2} a^{-1} $decade^{-1}$, $P < 0.05$), with growth varying by scenario and there is regional heterogeneity; the first principal mode of GPP was positive in most areas (59.55% to 100%), with the same increasing and decreasing characteristics; the spatial centroid of GPP exhibited a shift from the east and south toward the west and north, accompanied by marked ecosystem greening; extremely high temperature exerted the most -substantial negative influence on GPP under SSP5-8.5 (standardized path coefficients: −0.580), whereas extreme precipitation duration in SSPs 1-2.6 and 3-7.0, and intensity in SSP2-4.5. The total effect of extreme events on GPP change shifts from a positive to a negative effect (0.966 → −0.655, −167.81%) with increasing carbon emissions. Negative effects are concentrated in Northeast China, East China shows alternating positive and negative effects, and the other regions shift from positive to negative effects. This study emphasizes the importance of differentiated climate change adaptation capacity building.

Introduction

Global terrestrial ecosystems absorb ~30% of annual anthropogenic carbon emissions [1], with an average sink of 2 Pg C/a over the past century [2]. Extreme climate events alter plant carbon sinks by altering their high-temperature absorption and water availability, affecting the gross primary production (GPP) of vegetation [3]. Over the past 40 years, shifts from greening to browning have been widespread [4]. Understanding how extreme events trigger productivity losses in terrestrial ecosystems is essential.

Extreme precipitation–high-temperature events are the 2 main types of extreme climate events that intensify GPP variability in terrestrial ecosystems [5], with negative impacts on northern midlatitude ecosystems increased by 10.6% during 2000 to 2016 relative to 1982 to 1998 [6], and inducing pulsed, persistent stress [7]. Extreme precipitation impacts vegetation carbon sequestration [8], while secondary hazards (e.g., storm surges and floods) disrupt ecosystem health, causing vegetation mortality and reducing productivity in 51% of global wet ecosystems [9]. High temperatures inhibit photosynthesis, accelerate respiration, and disrupt cell membranes, reducing vegetation productivity, hydrological regulation, and ecological carbon sinks while increasing pest outbreaks, diseases, fires, and vegetation mortality [10]. For instance, the extremely high temperatures in 2022 reduced the net carbon sink of European forests by an estimated 56 to 62 Tg C [11]. Although the adverse effects of extreme precipitation or high temperature on GPP are well documented, our understanding of the impacts produced by consecutive or simultaneous extremes in terrestrial ecosystems remains limited.

Over the past few decades, China's large-scale ecological restoration programs have markedly reshaped GPP across its terrestrial ecosystems. Can extreme climatic events offset or reverse the rising trend in vegetation productivity? Attribution analyses capture complex patterns, while ecosystem models incorporating high-quality meteorological–ecological data isolate climate–vegetation interactions and illuminate the impacts of extreme events [12]; process-based models demonstrate that the increase in annual total GPP of terrestrial ecosystems in China was mainly influenced by the changes in vegetation structure from 2001 to 2016 [13]. Extreme-gradient-boosting analysis shows that, on 0.5 to 3 h time scales, regional GPP variability is chiefly driven by diffuse short-wave radiation [14], and random forest model simulations showed that changes in soil moisture content led to the GPP decline in China. However, the black box nature of machine learning may mask the true mechanisms of influence. Causal analysis methods have advantages in revealing the physical relationships between ecosystem processes and variables, including structural equation modeling (SEM), convergent cross-mapping [15], and directed acyclic graph [16]. For example, SEM-based methods found that net radiation affected both net ecosystem exchange and GPP in the Huaihe River Basin at multiple time scales. SEM clarifies the pathways through which multiple factors affect GPP, quantifies their individual contributions, and excels at disentangling complex relationships and supporting multigroup comparisons. Despite advances in attribution methods, spatiotemporal uncertainties persist in linking extreme precipitation and high-temperature events to terrestrial ecosystem changes under climate change, complicating the accurate quantification of their dynamic impacts on GPP in Chinese ecosystems. The analysis system combining structural equation model, empirical orthogonal function, and center of gravity shift models can systematically analyze the spatiotemporal interaction evolution mechanism of GPP at the national regional scale from 1981 to 2100, extract its dynamic and spatial heterogeneity characteristics at multiple time scales, clarify the impact path and contribution of extremely high-temperature precipitation events on GPP changes, and provide data support for strengthening differentiated extreme climate change adaptation capacity building and constructing a resilient ecological system for national land space.

This study fuses GPP and climate data from 4 shared socioeconomic pathway (SSP) scenarios for 1981 to 2100 and use SEM to analyze the impact path of the frequency, intensity, and duration/total days of extreme precipitation–high-temperature events on GPP changes in terrestrial ecosystems in China, quantifying their impact size to elucidate the response of vegetation to compound extremes, and providing key quantitative data for clarifying the differential mechanism of extreme climate events on GPP in terrestrial ecosystems. The objectives are to (a) quantify temporal GPP trends with the Sen-Slope estimator and Mann–Kendall test, and characterize spatial heterogeneity; (b) extract main spatiotemporal modes via empirical orthogonal function (EOF) analysis; (c) track GPP redistribution with a center-of-gravity shift model; and (d) assess the direct and indirect impacts of concurrent extreme precipitation–high-temperature events on GPP using the SEM method. This study aims to provide an integrated modeling framework for assessing vegetation dynamics under extreme climate events and underpin integrated climate–ecosystem security strategies.

Materials and Methods

China's geographic/climatic characteristics and regional division

China's topography features a west-to-east terraced gradient, characterized by substantial elevation differences (−268 to 8,405 m), diverse geographic and climatic conditions (Fig. 1), and marked latitudinal variation in annual precipitation (58.09 to 2,820.68 mm) and mean annual temperature (−1.44 to 27.80 °C). Based on the principle of climate–geography similarity, China was divided into 6 regions: North (NC), Northwest (WC), Northeast (NEC), Southwest (SWC), East (EAC), and South Central (SC).

Data sources and processing methods

Following the principle of universality in climate research [17], the study adopts the climate baseline period (1981 to 2010) as the historical reference, while the future period (2011 to 2100)

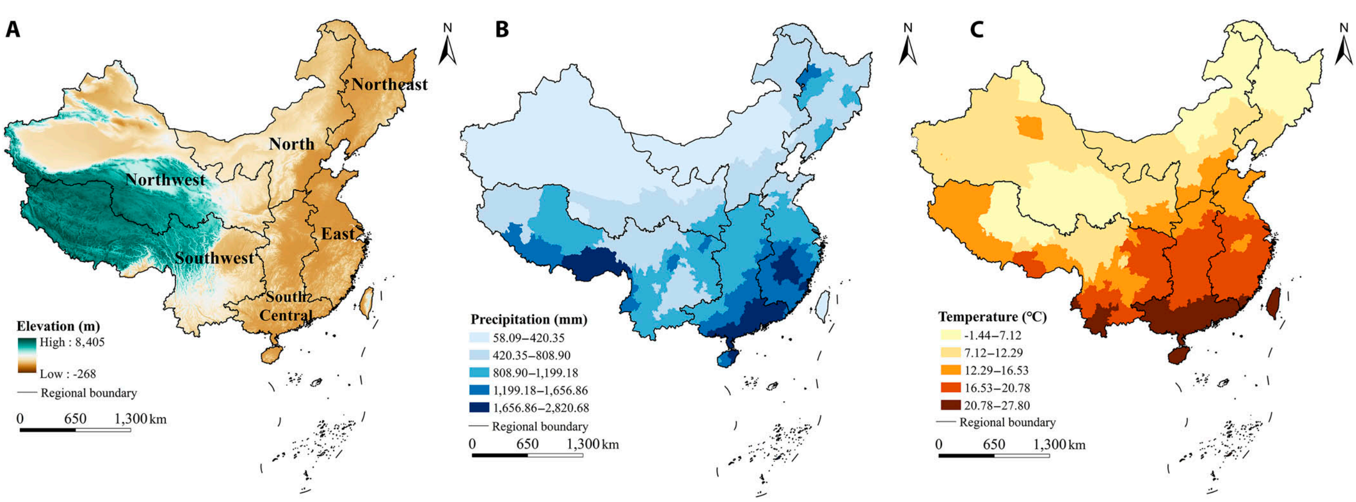

Fig. 1. Elevation and regional division in China [(A) North (NC), Northwest (NWC), Northeast (NEC), Southwest (SWC), East (EAC), and South Central (SC)], average precipitation in 2023 (B), and average temperature in 2023 (C). China map: GS (2024) 0650 (Ministry of Natural Resources).

is analyzed under 4 SSP scenarios, representing socio-economic trajectories ranging from low-carbon development to high fossil fuel consumption [18]. The Global Climate Models (GCMs) review has confirmed the superiority of the BCC-CSM2-MR model (Table S1) in simulating GPP and extreme events in China, with a correlation of up to 0.998 ($P < 0.05$) [19]. GPP products (https://aims2.llnl.gov/search/cmip6/) and 13 extreme precipitation–high-temperature indices (Table S2, https://cds.climate.copernicus.eu/datasets/sis-extreme-indices-cmip6?tab=overview) were used to represent nexus relationship. The GPP remote sensing inversion product (0.25° × 0.25°, 1988 to 2020) was obtained from the VODCA2GPP dataset. Evaluation using MODIS and TRENDY-v7 GPP data showed that the overall performance of VODCA2GPP was robust, with correlations of 0.53 and 0.61, respectively [20]. Temperature–precipitation data for China (2023, https://www.ncei.noaa.gov/data/global-summary-of-the-day/archive/) were used to describe the current status of regional climate differences, and elevations and administrative zones were used to qualitatively analyze regional climate–society relationships (https://www.resdc.cn/). GPP data were extracted by batch masking using "Python 3.10" (https://www.python.org/), and then it was downscaled (0.25°×0.25°, consistent with the extreme indices) using a bilinear interpolation method [21], thereby improving spatial resolution while suppressing the influence of anomalies [22].

Methods

Performance evaluation of GCMs

This study uses root mean square error (RMSE) to evaluate the average correlation between historical BCC downscaled products and VODCA2GPP data (Eq. 1) [23].

$$\mathrm{RMSE} = \sqrt{1/n * \sum_{i=1}^{n} \left(x_{y,i} - x_{z,i}\right)^2} \tag{1}$$

where n is the amount of data, $x_{y,i}$ is the measured value, and $x_{z,i}$ is the model simulation value. Therefore, low RMSE values represent good model performance.

Detecting spatiotemporal changes in GPP

First, the nonparametric Sen slope is used to quantify the temporal changes in GPP for each grid cell from 1981 to 2100, and their significance was tested using the Mann–Kendall method (Eqs. 2 to 5). These methods effectively preserve spatial heterogeneity, making them widely applicable in vegetation dynamics research [24].

$$\mathrm{SL} = \mathrm{Median}\left(\frac{z_a - z_b}{a - b}\right), a > b \tag{2}$$

$$S = \sum_{i=1}^{n-1} \sum_{i=k+1}^{n} \mathrm{sign}\left(x_i - x_k\right) \tag{3}$$

$$\mathrm{sign}\left(x_i - x_k\right) = \begin{cases} 1, & \left(x_i - x_k\right) > 0 \\ 0, & \left(x_i - x_k\right) = 0 \\ -1, & \left(x_i - x_k\right) < 0 \end{cases} \tag{4}$$

$$z = \begin{cases} \dfrac{S-1}{\sqrt{\mathrm{Var}(S)}}, & S > 0 \\ 0 & \\ \dfrac{S+1}{\sqrt{\mathrm{Var}(S)}}, & S < 0 \end{cases} \tag{5}$$

where SL is the slope, z_i is the data at position i in the time series, a and b are the sequence positions, and Median() is the median-taking function. Var(S) is the variance of the indicator S ($P <$ 0.05, $|Z|$ standardized value of 1.96). A significant increasing (SL > 0) or decreasing (SL < 0) trend occurs when $|Z| > 1.96$, and an increasing (SL > 0) or decreasing (SL < 0) trend occurs when $|Z| < 1.96$. The above calculations were implemented using the "pymannkendall" package for Python 3.10.

Second, the temporal nonlinear characteristics and long-term phase changes of the trend were analyzed. EOF based on singular value decomposition theory [25] was employed to extract the main spatial patterns and corresponding time coefficients of the GPP dataset from its spatial covariance matrix (Eqs. 6 and 7). The EOF analysis was used to reveal the main spatial variability patterns [26], which were evaluated using the North criteria to ensure independence [27].

$$X(s,t) = \sum_{n=1}^{N} a_n(t)\varphi_n(s) + \varepsilon(s,t) \tag{6}$$

$$\Delta\lambda_k = \lambda_k \sqrt{\frac{2}{n^*}} \tag{7}$$

where $X(s,t)$ denotes the input data, and s and t denote the spatial and temporal dimensions, respectively; $a_n(t)$ is the time coefficient of the nth EOF, $\varphi_n(s)$ corresponds to its spatial distribution, and the error term $\varepsilon(s,t)$ denotes the residuals that are not explained by the patterns; the range of the eigenvalue error $\Delta\lambda$ is used to assess the separability between the patterns, λ_k denotes the eigenvalue of the kth EOF pattern, and n^* denotes the effective degree of freedom. EOF analysis involved computing the spatial covariance matrix and decomposing its eigenvalues. In this study, pattern independence and statistical were determined based on nonoverlapping $\Delta\lambda$ values between adjacent eigenvalues: if $\lambda_k \pm \Delta\lambda_k$ and $\lambda_{k+1} \pm \Delta\lambda_{k+1}$ do not overlap, the modes are deemed independent and statistically significant. The calculations were performed using the "Eof" package in Python 3.10.

Finally, the spatial statistics and probability density estimation methods provided by ArcGIS 10.7 were used to reveal the concentrated/discrete status of the distribution of GPP; combined with the center of gravity shift model to calculate the trajectory of GPP, the model represents the point of synergistic force and spatial concentration generated by the distribution of elements [28].

Attribution analysis of GPP

First, the Pearson correlation coefficient ($-1 \le r \le 1$) was utilized to evaluate the response of 13 precipitation–high-temperature indices to GPP in China from 1981 to 2100. The coefficient r less than 0 is a negative correlation, and that higher than 0 is a positive correlation; a larger $|r|$ signifies a stronger correlation ($P < 0.05$) [29].

SEM quantifies the comprehensive impact of variables from extreme precipitation–high-temperature events on GPP of terrestrial ecosystems [30]. This method allows the construction of latent variables and the analysis of nonintuitive causal chains based on multiple observation indicators. First, assume that frequency, intensity, and duration/total days of both extreme precipitation events and extremely high-temperature events directly impact GPP. Accordingly, a conceptual model of the causal relationship between these extreme event indicators and GPP is constructed. The conceptual model is then transformed into a structural equation model (Eqs. 8 to 10). Input observation variables are grouped as follows: GPP; for extreme precipitation events—frequency (R10MM, R20MM, and SDII), intensity (RX1DAY, RX5DAY, and CWD), and duration/total days (PRCPTOT, R95P, and R99P); for extremely high-temperature events—frequency (TX90P), intensity (TXX and TXN), and duration/total days (WSDI) [31,32]. The indicators were calibrated according to fit indices and the best-fit model using the chi-square test (χ^2)/degrees of freedom (df) and root mean square error of approximation (RMSEA) (Eqs. 11 and 12).

$$y = \beta_0 + \sum_{i=1}^{n} \beta_i x_i + \varepsilon \tag{8}$$

$$\begin{bmatrix} 1 & r_{x_1x_2} & \cdots & r_{x_1x_n} \\ r_{x_2x_1} & 1 & \cdots & r_{x_2x_n} \\ \vdots & \vdots & \ddots & \vdots \\ r_{x_nx_1} & r_{x_nx_2} & \cdots & 1 \end{bmatrix} \begin{bmatrix} w_1 \\ w_2 \\ \vdots \\ w_n \end{bmatrix} = \begin{bmatrix} r_{x_1y} \\ r_{x_2y} \\ \vdots \\ r_{x_ny} \end{bmatrix} \tag{9}$$

$$r_{x_iy} = \beta_i + r_{x_ix_1}\beta_1 + r_{x_ix_2}\beta_2 + \cdots r_{x_ix_j}\beta_j \cdots + r_{x_ix_n}\beta_n \tag{10}$$

$$\chi^2 / df = \frac{(n-1) \bullet F_{\mathrm{FIML}}}{df} \tag{11}$$

$$\mathrm{RMSEA} = \sqrt{\frac{\max\left(\chi^2 - df, 0\right)}{df(n-1)}} \tag{12}$$

where y is the dependent variable, β_0 denotes the expected value of y when all independent variables x_i are 0, β_i is the regression coefficient of x_i, and the error term ε represents the unexplained random variation in the model. The path coefficient between variables and GPP changes is the standardized regression coefficient. The larger the path coefficient, the greater the impact of variables on GPP changes. r_{x_iy} is the total correlation coefficient between x_i and y, which represents the combined effect of x_i on y. $r_{x_ix_j}$ denotes the correlation coefficient between x_i and x_j. w_i is the standardized regression coefficient, which represents the direct effect of x_i on y when the correlation of other variables is taken into account. n is the sample size, df is the degree of freedom, and F_{FIML} is the minimum value of the full information maximum likelihood estimation. The model passes the goodness-of-fit test when the RMSEA is close to 0 and $\chi^2/df < 5$ [33]. SEM calculations were implemented using the "semopy" packages of Python 3.10. The above data processing and modeling methods were combined for the analysis of this study (Fig. 2).

Results

Performance evaluation of GCMs

The downscaled outputs of the extreme climate indices and the reanalysis data for the historical period (1981 to 2010) agree well, with the average Pearson correlation coefficient greater than 0.6 [34]. There is good consistency between the GPP downscaled output of BCC and the VODCA2GPP data (Fig. S1). The national average RMSE value is 2.96 kg C m^{-2} a^{-1}, and the overall simulation performance of GPP in NWC is the best; the regional average RMSE value is 2.27 kg C m^{-2} a^{-1}.

Temporal variability of GPP

During the study period, GPP values exhibited a right-skewed distribution characterized by an increase, with more values

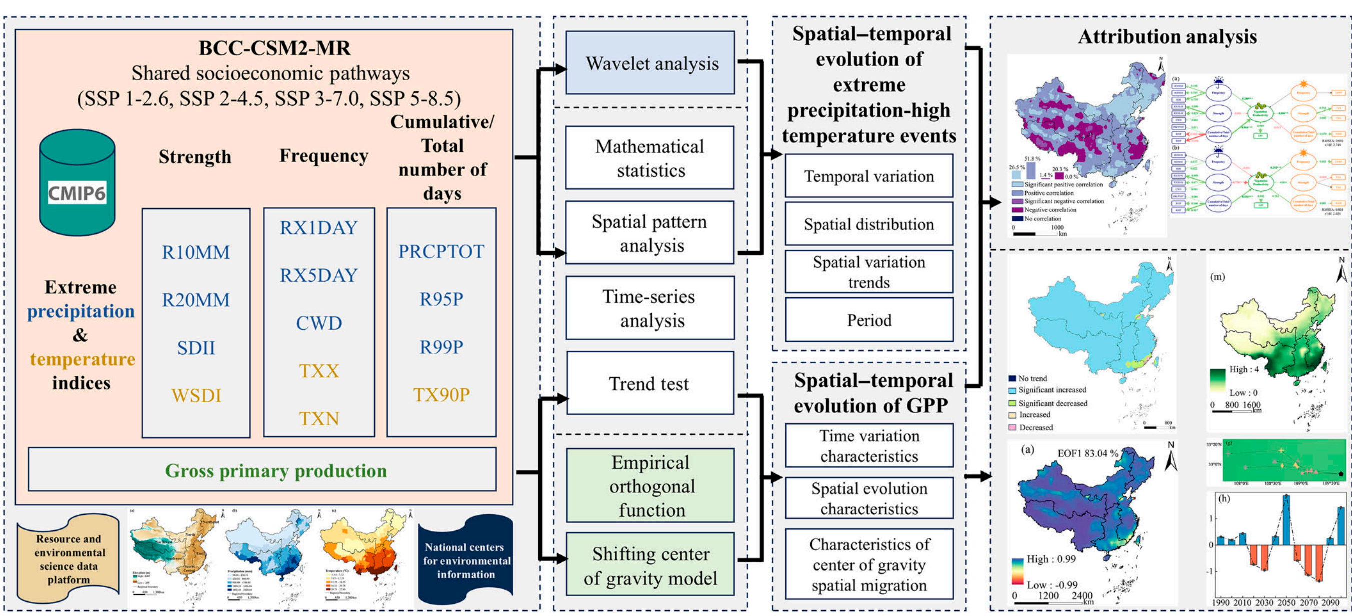

Fig. 2. The integrated assessment framework of this study. China map: GS (2024) 0650 (Ministry of Natural Resources).

above the third quartile and below the first quartile under high-emission scenarios (SSPs 3-7.0 and 5-8.5). An increase trend was observed in the mean value of GPP as a whole (0.19 to 0.80 kg C m^{-2} a^{-1}, SL > 0, $R^2 > 0.7$) with a significant increase ($R^2 > 0.9$) in SSP5-8.5 (129.18%) and SSP3-7.0 (108.09%). From 2041 to 2070, the gap between scenarios widens and GPP accelerates most under SSP3-7.0 and SSP5-8.5, yet it still increases significantly across >97% of China, with declines confined to a handful of scattered patches—the southern, northeastern, and eastern EAC (SSP1-2.6 and/or SSP3-7.0); the southern NC, SC, and EAC (SSP1-2.6); portions of the NWC (SSP1-2.6 and SSP2-4.5); and a few isolated northern sites (Fig. 3). While a widespread, long-term increase in GPP was observed nationwide, there is still substantial regional heterogeneity, with certain areas like the EAC and SC experiencing declines under the SSP1-2.6 scenario.

The first principal mode (PC1) of the EOF analysis shows a marked "negative and then positive" upward trend in GPP (Fig. 4), consistent with the "Sen-Slope + Mann–Kendall" test, confirming China's GPP growth potential. GPP growth accelerates after 2031 under SSP1-2.6, while the inflection points for high-emission scenarios are delayed to 2041 (SSP2-4.5) and 2051 (SSPs 3-7.0 and 5-8.5). The second principal mode (PC2) captures temporal fluctuations, with alternating positive–negative changes and greater variability than PC1, showing interdecadal shifts. In SSP1-2.6, GPP peaks positively in 2021 and 2051, with negative inflection points in 1991, 2041, and 2061. SSP2-4.5 displays 10- to 20-year cycles, while SSP3-7.0 shows a single positive peak in 2091 with low volatility. SSP5-8.5 advances its positive inflection to 2081. SSP1-2.6 exhibits earlier growth acceleration and regular oscillations, while SSP5-8.5 shows delayed trends with greater fluctuations.

Spatial distribution and migration of GPP

GPP displayed a pronounced north–south contrast, being higher in the south and lower in the north (Fig. 5). Substantial increases occurred in the south-central SW, southeastern NWC, and southern NEC, SC, and EAC, while the low-value (<1.5 kg C

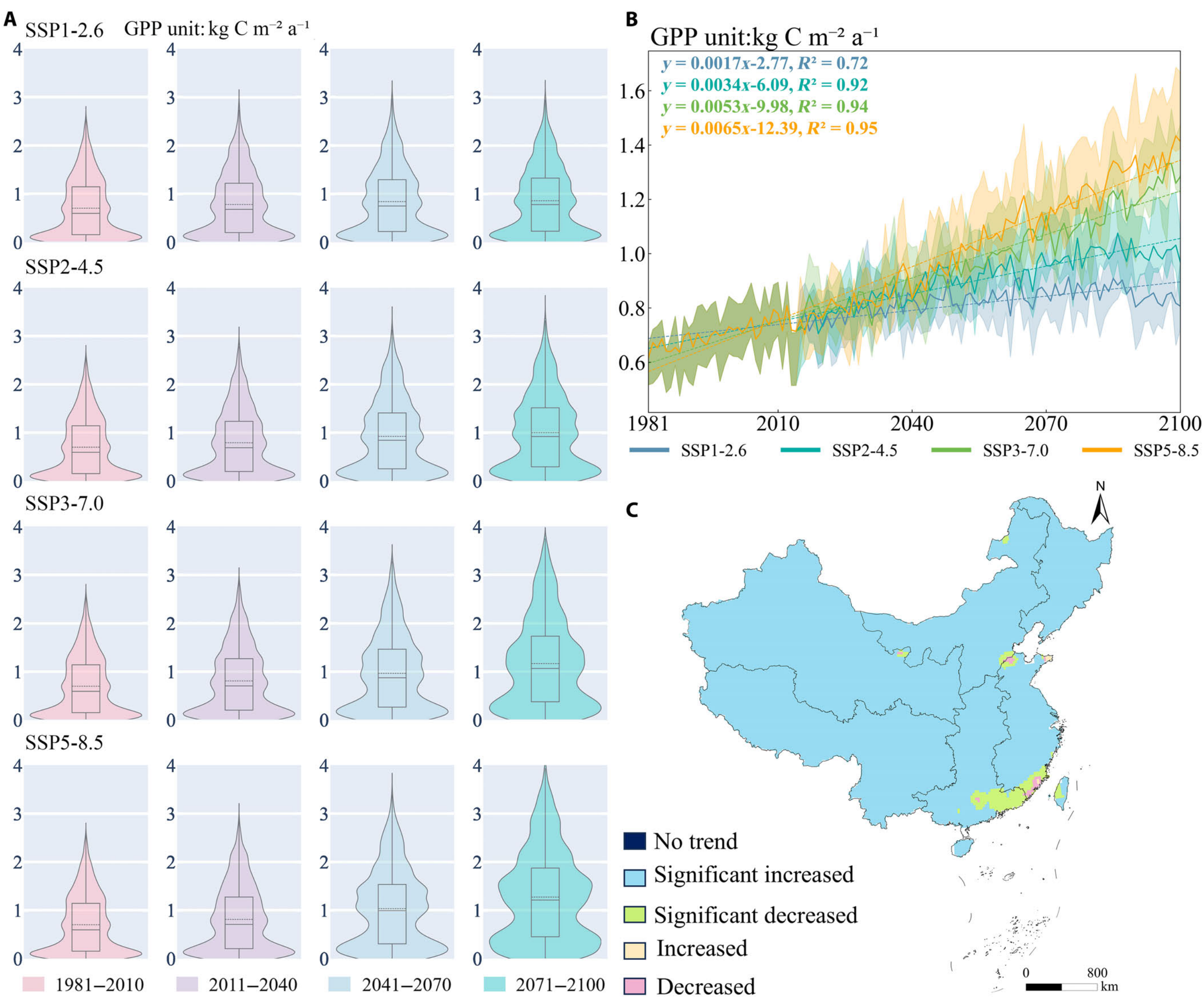

Fig. 3. Violin statistics (A), temporal [(B) shaded intervals are median and 60th percentile], and spatial trends [(C) SSP1-2.6 is as an example, North (NC), Northwest (NWC), Northeast (NEC), Southwest (SWC), East (EAC), and South Central (SC)] of GPP in China under 4 scenarios, 1981 to 2100. China map: GS (2024) 0650 (Ministry of Natural Resources).

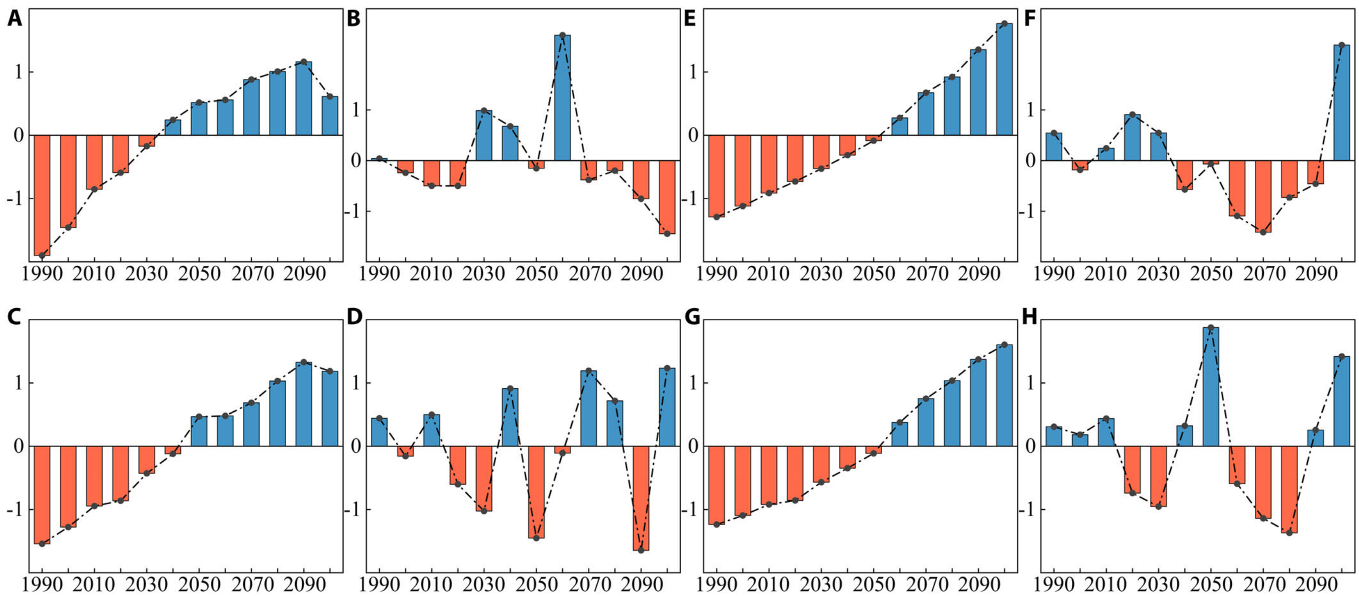

Fig. 4. Time coefficients of the first (PC1) and second (PC2) principal modes of GPP under the scenarios of SSP1-2.6 [(A) PC1; (B) PC2], SSP2-4.5 [(C) PC1; (D) PC2], SSP3-7.0 [(E) PC1; (F) PC2], and SSP5-8.5 [(G) PC1; (H) PC2].

m^{-2} a^{-1}) zone in eastern and northern NC narrowed. Between 2011 and 2040, the low-value zone in central SC expanded under SSP1-2.6, while it contracted in southwestern EAC and central SC under other scenarios. From 2041 to 2070, high-value zones (>2.5 kg C m^{-2} a^{-1}) expanded in southern mountains, northern SWC, southeastern SC, and southern EAC, with SSP1-2.6 showing the lowest expansion. By 2071 to 2100, GPP increased in southern NWC, EAC, central SWC, southwestern SC, and northern NEC, with SSP5-8.5 showing the largest magnitude and extent of increase. The pattern of the spatial distribution of GPP in SSP5-8.5 and SSP3-7.0 (2041 to 2070) is close to the GPP pattern in SSP2-4.5 (2071 to 2100). SSP1-2.6 differs from the other scenarios from 2040 onwards, but with a low increase.

EOF1 explains 83.04% to 96.85% of GPP's spatial variation, increasing with higher-emission scenarios (Fig. 6), while EOF2 contributes the most under SSP1-2.6 (4.35%) and least under SSP3-7.0 (0.98%). The 2 modes cumulatively explain 87.39% to 97.96% of the variance, with EOF1 capturing the dominant GPP pattern. EOF1 is positive nationwide and strengthens from SSP1-2.6 to SSP5-8.5, peaking in western and southern SWC and weakening toward the east and north, thereby recapitulating the long-term mean GPP pattern. Negative values are mainly in southern SC and EAC, with scattered northern areas under SSP2-4.5, clustered in NEC and NWC under SSP3-7.0. The primary mode is climate-driven, while the secondary mode reflects ecological risks in northern sensitive and southern subtropical regions. EOF2 exhibits greater spatial heterogeneity, with north–south divergence increasing under higher-emission scenarios. In SSP1-2.6, positive high-value areas are in southeastern EAC, southern NC, and western SWC, while negative high-value areas are southern regions, eastern NC, and NEC. Under SSP2-4.5, negative areas in southern regions decrease and shift to low-latitude subtropical areas, while positive areas are concentrated in NC and northern NWC, and shift from positive to negative in southeastern EAC. In SSP3-7.0, negative areas expand, with clusters in NEC, central NWC, and southern SC, while positive high values occur in central and northern NC, with negative areas exceeding positive areas. Under SSP5-8.5, positive areas have the lowest extreme values, and negative areas are concentrated in the south.

The GPP center shifts westward and northward, with amplitude following SSP5-8.5 > SSP-7.0 > SSP24.5 > SSP1-2.6. This shift indicates a gradual migration of GPP concentration from densely vegetated eastern and southern regions to sparsely vegetated western and northern regions, suggesting an overall improvement in terrestrial ecosystems nationwide (Fig. 7). Regionally, the NEC shifts eastward overall but briefly moves westward under SSP3-7.0 (2011 to 2040) and SSP2-4.5 (2071 to 2100). The NC primarily moves northward and westward, while the EAC shifts southward and slightly westward (SSP3-7.0 > SSP5-8.5 > SSP2-4.5 > SSP1-2.6). The NWC migrates mainly westward, with similar amplitudes for SSPs 1-2.6 and 2-4.5. The SWC shifts west and north, but moves southeast under SSP1-2.6 (2071 to 2100). In SC, GPP shifts are generally westward, with brief eastward and northward trends under SSP1-2.6 (2041 to 2070). Northern regions shift slightly southward due to resource limitations, while southern regions shift northward, influenced by warming. SSP5-8.5 shows larger migration magnitudes, while low-emission scenarios exhibit smaller shifts.

Correlations between extreme events and GPP

Across China, more than 87% of regions exhibit a statistically significant positive correlation between extreme-climate indices and GPP (Figs. S2 and S3), and only a few regions in the northwestern part of NWC, the southern part of EAC, and the eastern part of EAC showed positive correlation (<15%) or negative correlation (<5%) between CWD and GPP (Fig. S2), with significant positive correlation areas (26.5%) concentrated in NC and NEC, and negative correlation (20.3%) and significant negative correlation areas (1.4%) concentrated in NWC and SWC. Extremely high-temperature indices have a more generalized significant positive correlation with GPP, and extreme

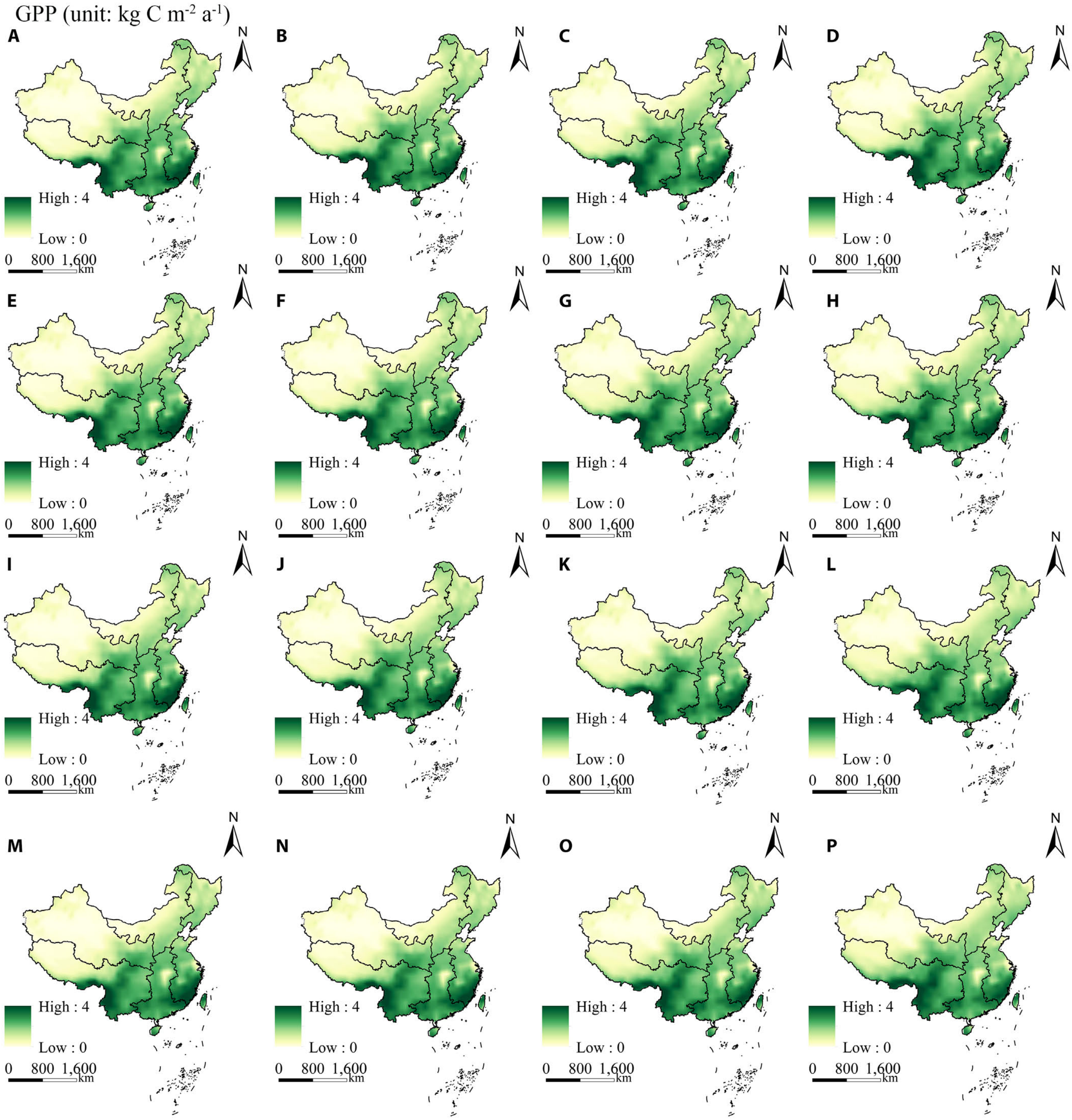

Fig. 5. Spatial distribution of GPP under the scenarios of SSP1-2.6 [(A) 1981 to 2010; (B) 2011 to 2040; (C) 2041 to 2070; (D) 2071 to 2100], SSP2-4.5 [(E) 1981 to 2010; (F) 2011 to 2040; (G) 2041 to 2070; (H) 2071 to 2100], SSP3-7.0 [(I) 1981 to 2010; (J) 2011 to 2040; (K) 2041 to 2070; (L) 2071 to 2100], and SSP5-8.5 [(M) 1981 to 2010; (N) 2011 to 2040; (O) 2041 to 2070; (P) 2071 to 2100] in China, 1981 to 2100. China map: GS (2024) 0650 (Ministry of Natural Resources).

precipitation frequency (R10MM) and intensity (RX1DAY, RX5DAY, SDII, and R99P) are more than the duration/total number of days (R20MM, PRCPTOT, and R95P) and exhibited a more generalized significant positive correlation with GPP.

Impact pathways of extreme events on GPP

The 13 extreme climate indices in China generally increase, rising with higher-emission scenarios (Fig. 8 and Table S3). The best SEM fit (RMSEA < 0.005, χ^2/df < 5) shows that under SSP1-2.6, changes in GPP are driven by extreme precipitation (duration/total days: R95P, R99P, and PRCPTOT), with a path coefficient of 0.966 ($P < 0.001$). Extreme precipitation frequency (R10MM, R20MM, and SDII) and temperature intensity (TXX and TXN) showed smaller positive effects. In SSP2-4.5, extreme precipitation intensity (RX1DAY, RX5DAY, and CWD) had the largest negative impact on GPP (−0.778, $P < 0.001$), while duration/total days (0.531) and high-temperature frequency (TX90P: 0.292) had positive effects. Negative impacts

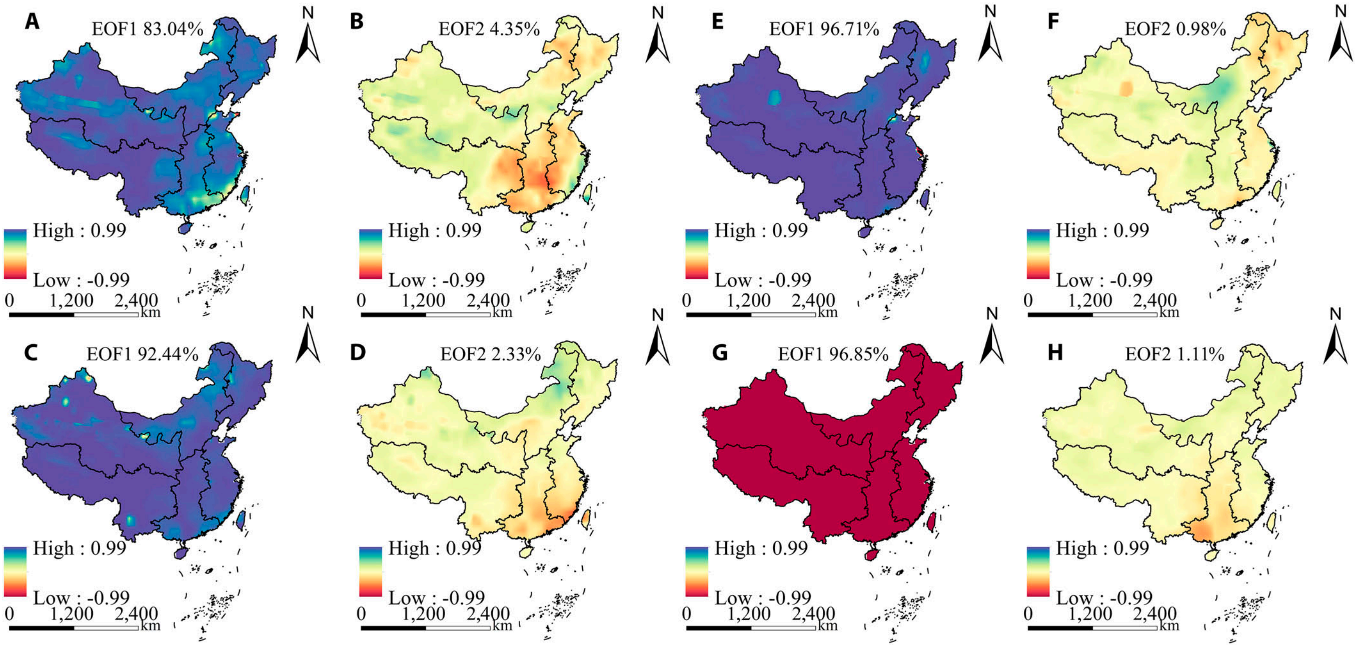

Fig. 6. Spatial distribution of the principal modes of GPP under the scenarios of SSP1-2.6 (A and B), SSP2-4.5 (C and D), SSP3-7.0 (E and F), and SSP5-8.5 (G and H) in China, 1981 to 2100. China map: GS (2024) 0650 (Ministry of Natural Resources).

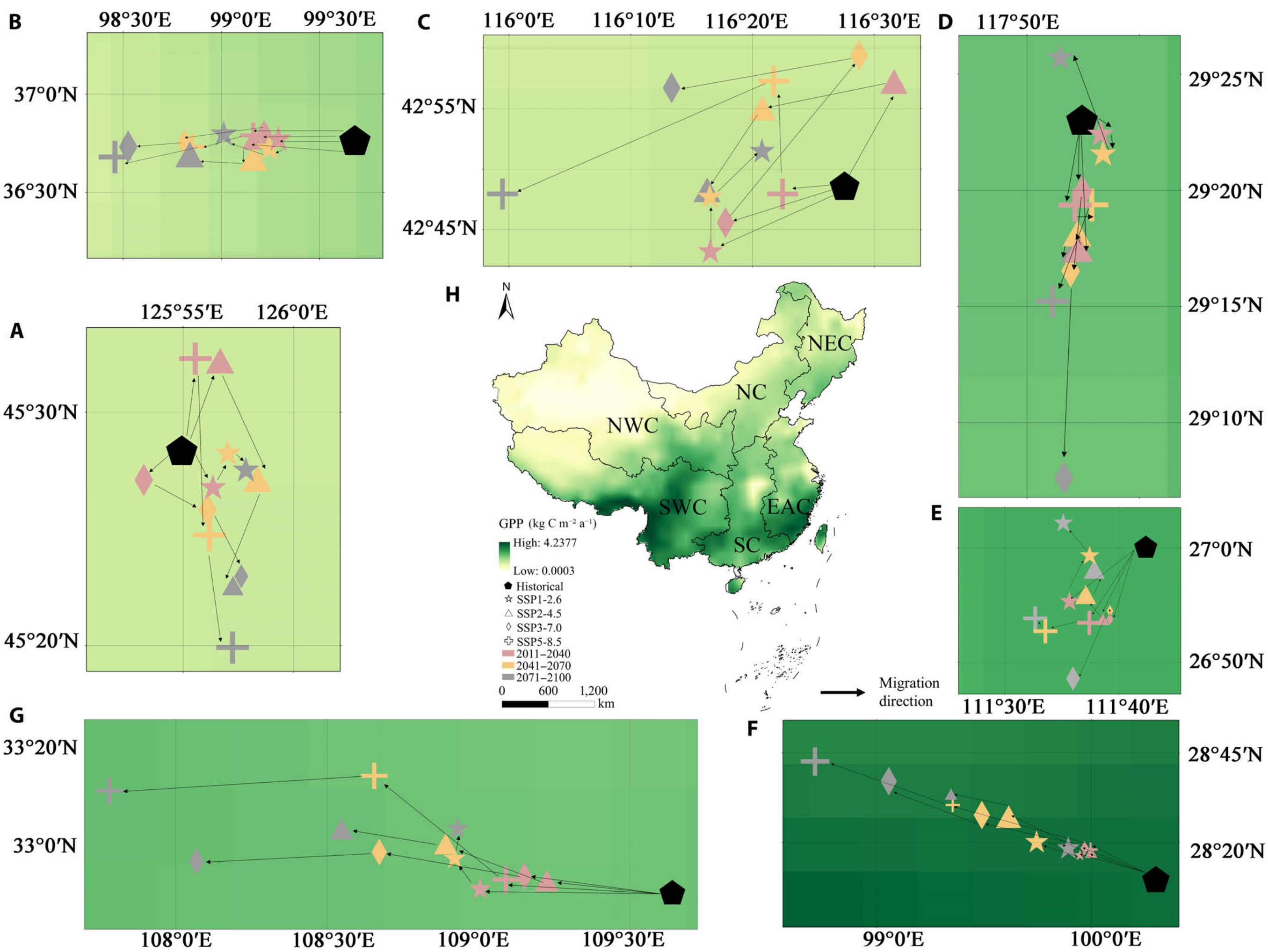

Fig. 7. The trajectory of GPP's center of gravity in China [(A) Northeast, NEC; (B) Northwest, NWC; (C) North, NC; (D) East, EAC; (E) South Central, SC; (F) Southwest, SWC; (G) China; (H) 2071 to 2100 (SSP5-8.5)] under 4 scenarios, 1981 to 2100. China map: GS (2024) 0650 (Ministry of Natural Resources).

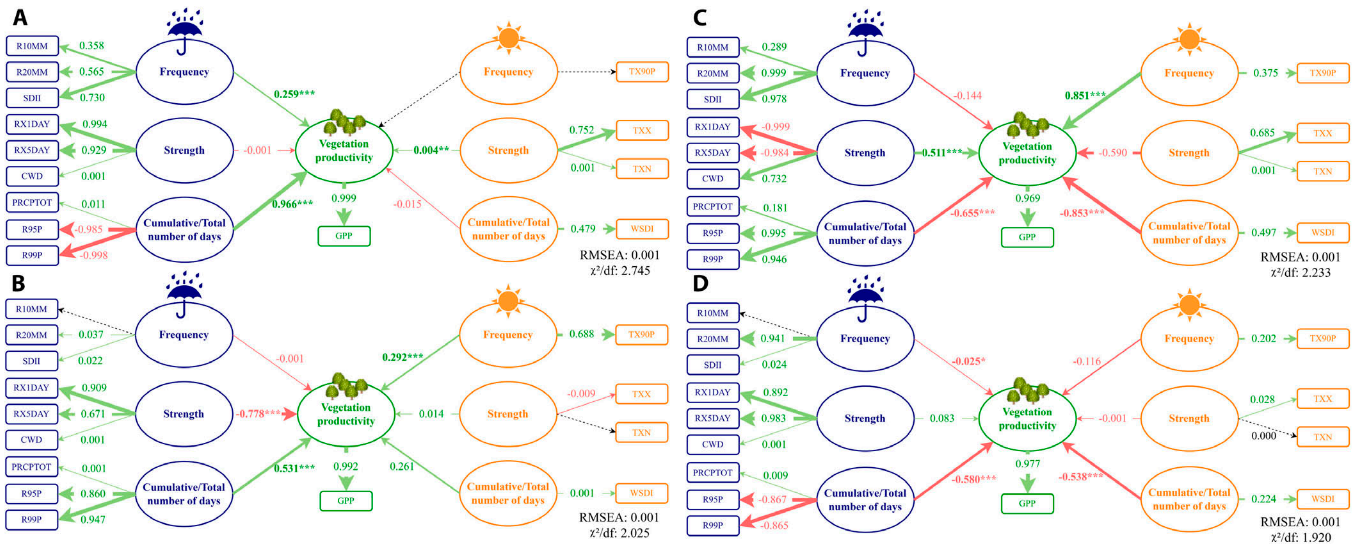

Fig. 8. Relationship between extreme precipitation, high temperature, and GPP nationwide under the scenarios of SSP1-2.6 (A), SSP2-4.5 (B), SSP3-7.0 (C), and SSP5-8.5 (D). Thickness represents normalized path coefficients. Blue (precipitation) and yellow (temperature) arrows indicate factors, with green lines for positive effects, red lines for negative effects, and dashed lines for nonsignificant paths at different significance levels (*$P < 0.1$, **$P < 0.01$, and ***$P < 0.001$). Latent variables are circled, and observed variables are boxed.

grew under SSP3-7.0, but high-temperature frequency (0.851) and precipitation intensity (0.511) became strongly positive. Under SSP5-8.5, GPP change is largely negative, with duration/total days having the strongest negative effects (precipitation: −0.580, high-temperature: −0.538, $P < 0.001$), followed by precipitation frequency. As extreme-climate indices climb from SSP1-2.6 to SSP5-8.5, extreme precipitation flips from a positive to a negative influence on GPP, while high-temperature impacts become increasingly detrimental.

Regionally, extreme weather indices increase across most of China from 1981 to 2100, except for declines in parts of SWC. Extreme precipitation–high-temperature events rise in southeastern NC, northeastern SWC, and NWC; high temperatures intensify in southwestern NEC, while SC, south-central EAC, and coastal regions face more extreme precipitation. China is projected to experience hotter, more humid conditions [34]. The impact of extreme precipitation–high temperature on GPP varies markedly across regions (Fig. 9 and Figs. S4 to S6). SEM models under all 4 scenarios are validated.

In the EAC, extreme precipitation positively affected GPP under SSP1-2.6, driven by precipitation duration (0.512, $P < 0.001$) and intensity. Under SSP2-4.5, high-temperature intensity had a negative effect (−0.182), outweighing the positive effect of high-temperature duration (0.103). In SSP3-7.0, high-temperature frequency positively impacted GPP (0.545), but the effect of duration shifted from positive to negative. Precipitation duration still has a greater impact under SSP5-8.5, while high-temperature frequency negatively affected GPP (−0.027). In the SWC, under SSP1-2.6, precipitation frequency had a significant negative effect (−0.753), while in SSP2-4.5, precipitation–high-temperature events had a positive impact, led by precipitation intensity (0.933). In the NC, effects mirrored the NWC: positive impacts under SSP1-2.6, but negative under SSP5-8.5; precipitation intensity shifted to a negative effect (−0.453), and high-temperature frequency worsened impacts (−0.316, $P < 0.1$) in SSP3-7.0; under SSP5-8.5, high-temperature intensity (−0.532, $P < 0.001$) and frequency (−0.733) had significant negative effects. In the NEC, extreme precipitation–high-temperature events consistently negatively impacted GPP, driven by precipitation duration (SSPs 1-2.6 and 3-7.0), high-temperature duration (SSP2-4.5), and intensity (SSP5-8.5). In the SC, precipitation negatively affected GPP, with impacts driven by duration (SSPs 2-4.5 and 3-7.0), intensity (SSP5-8.5), and frequency (SSP2-4.5); positive effects were seen in SSP1-2.6, led by precipitation duration (0.967). In the NWC, SSPs 1-2.6 and 2-4.5 displayed positive impacts, dominated by high-temperature duration (0.277, $P < 0.1$) and precipitation intensity (−0.739, $P < 0.001$), with stronger effects in SSP2-4.5; negative impacts were detected by precipitation intensity (−0.985, $P < 0.001$) and high-temperature frequency (−0.568) in SSP3-7.0, and by high-temperature duration (−0.764) and frequency (−0.733) in SSP5-8.5.

Extreme precipitation and high temperature affect GPP in 3 patterns: consistently negative (NEC), positive under low emissions, but negative under high emissions (SC, NWC, NC, and SWC), and fluctuating between positive and negative (EAC). High temperature and the duration of precipitation dominate GPP changes in SSP5-8.5, while precipitation dominates in other scenarios. The duration/total days of extreme events has the strongest impact on GPP, likely due to cumulative stress exceeding vegetation tolerance [35]. SSP3-7.0 and SSP5-8.5 show compound negative effects in NWC, while SSP2-4.5 demonstrates positive synergies in the SWC, where moderate emissions create an ecological gain window, disrupted under high emissions.

In the NEC region, extremely high temperature and extreme precipitation have shown negative impacts on GPP in various scenarios. This may be due to the fact that NEC's ecosystem structure is dominated by northern or temperate forests with longer growth cycles, which are more susceptible to cumulative damage from long-term stress. In addition, legacy issues of land use, such as historical forest management or agricultural expansion, may amplify its sensitivity to extreme weather conditions. Under the SSP1-2.6 scenario, there is room for gain in GPP, indicating the necessity of early deployment of the "dual carbon" strategy, especially in optimizing the spatial layout of key urban agglomerations and assessing the impact of the "multidisaster

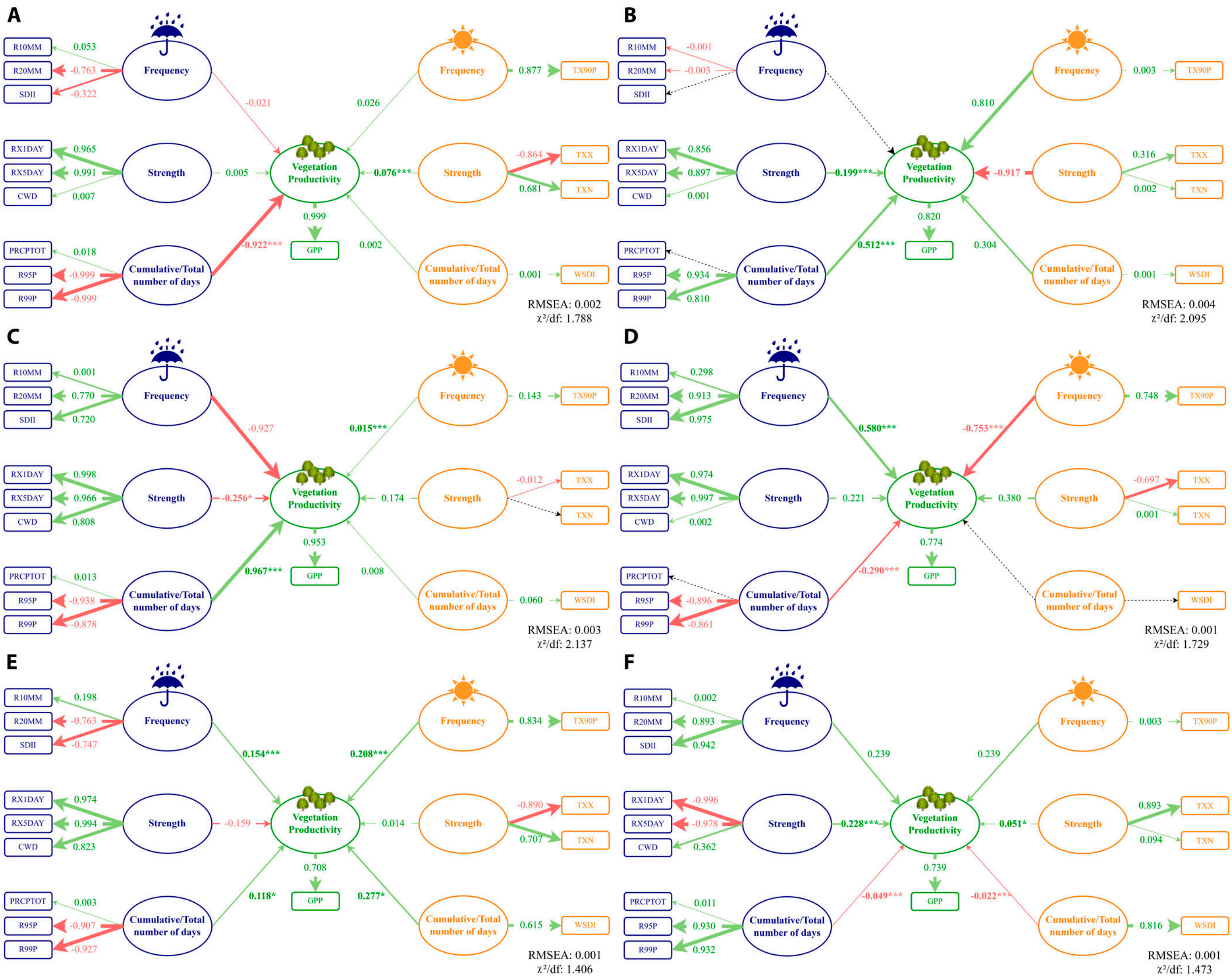

Fig. 9. Relationship between extreme precipitation, high temperature, and GPP in the EAC (A), SWC (B), NC (C), NEC (D), SC (E), and NWC (F) under SSP1-2.6. Thickness represents normalized path coefficients. Blue (precipitation) and yellow (temperature) arrows indicate factors, with green lines for positive effects, red lines for negative effects, and dashed lines for nonsignificant paths at different significance levels (**P* < 0.1, ***P* < 0.01, and ****P* < 0.001). Latent variables are circled, and observed variables are boxed.

chain", for example, evaluating the amplification effect of the synergistic changes of extreme precipitation, extremely high temperature, extreme drought, and wildfire on GPP in key regions, and continuously integrating models, data methods, and policy simulation needs. It is suggested to deepen the understanding of vegetation's response and tolerance to previous climate conditions, and combine methods such as nonlinear causal testing to further determine the lagged effects of potential factors on terrestrial ecosystem GPP.

Discussion

Drivers affecting changes in GPP

GPP changes are influenced by external meteorological conditions, atmospheric CO_2 levels, vegetation shifts, and human interventions [36]. For example, precipitation variability affects ecosystem productivity, with 49% of China's agroecosystems showing positive GPP–precipitation correlations [37]. Snow accumulation in wetter temperate regions delays the growing season and reduces spring GPP [38]. Soil moisture contributes increasingly to vegetation productivity by influencing water availability to roots [39]. Temperature has dual effects, enhancing photosynthesis and GPP in winter but reducing summer GPP under higher temperatures [40]. Increased solar radiation reduces GPP via stomatal closure under enhanced transpiration [13]. Extremely high temperature shows positive effects on GPP [41], while low-temperature events have negative impacts [42]. Elevated atmospheric CO_2 boosts photosynthetic capacity, influencing 51.11% to 90.37% of global forested areas [43]. In China, vegetation land-use changes increased carbon stocks by 1.32 Pg C between 2000 and 2018 [44]. Projects such as ecological water recharge contributed 60% of GPP growth in inland river basins, while the "Grain for Green" project drove GPP increases on the Loess Plateau [45]. Thus, GPP's spatial and temporal evolution reflects the interaction of atmospheric changes, vegetation dynamics, and management decisions.

Under SSP1-2.6, higher temperatures extend the growing season, enhance photosynthesis by increasing stomatal conductance [46], and, combined with extreme precipitation, improve soil water storage, aeration, and structure, accelerating greening [47]. In SSP2-4.5 and SSP3-7.0, negative effects intensify as high temperatures disrupt plant cellular structures and metabolic processes, while excessive soil water leads to stomatal closure, impaired root respiration, and premature leaf senescence [48]. SSP5-8.5 shows the strongest negative impacts, with strengthened water–temperature coupling [49]. By the late 21st century, extreme precipitation–high-temperature events dominate negative GPP extremes, outweighing the benefits of hotter, wetter conditions. This study provides a systematic assessment framework that improves characterization of extreme event impacts on GPP. The earliest GPP growth breakthrough under SSP1-2.6 is projected for 2031, highlighting the urgency of advancing the "dual-carbon" strategy. In particular, the optimization of spatial layout in key urban agglomerations and the assessment of the impact of "multihazard chains" should be given attention. For example, the amplification effect of the synergistic changes of extreme precipitation, extremely high temperature, extreme drought, and wildfire on GPP in key areas should be evaluated, and models, data methods, and policy simulation needs should be continuously integrated [50].

Spatiotemporal divergence of the GPP

EOF analysis under SSP5-8.5 shows that the first principal mode variance contribution increases from 76.70% in the historical period to 95.43% in the future (Fig. 10). EOF1 has had negative values in historical periods (such as the central NWC), while national EOF analysis from 1981 to 2100 shows that EOF1 is consistently positive. During the historical period of EOF2, it showed a spatial distribution of "positive in the west and negative in the east". In the future, only the southwestern region of SC will remain positive, while the national EOF analysis from 1981 to 2100 shows that EOF2 is positive in the north and negative in the southwestern region of SC. PC1 exhibits a "negative-then-positive" trend, indicating GPP growth, with accelerations in 2001 and after 2051. PC2 alternates between positive and negative, with substantial positive trends in 2001 and 2051, and negative change points in 1991, 2031, and 2081. Historical EOF analysis reflects combined natural variability and anthropogenic effects, while future EOF analysis (especially SSP5-8.5) highlights anthropogenic forcing. EOF analysis effectively identifies spatial modes and temporal coefficients of GPP, and future use of nonlinear EOF methods (e.g., Kernel principal component analysis) could better capture GPP thresholds under extreme climate events.

Principal mechanisms by which extreme events influence GPP

SEM analysis ($P < 0.01$; Fig. S7) shows that, under SSP5-8.5, extreme precipitation–high temperature exerted a pronounced negative influence on GPP during the historical period, driven by extremely high-temperature intensity (−0.445), extreme precipitation intensity (−0.330), frequency of extreme precipitation (−0.315), and duration/total days of extremely high temperature (−0.096). In the future, the factor shifts to the duration/total days of extremely high temperature (−0.586), outweighing the weak positive effects of high-temperature frequency (0.117) and extreme precipitation duration (0.186). Extremely high temperature generally exerts a stronger influence on GPP than extreme

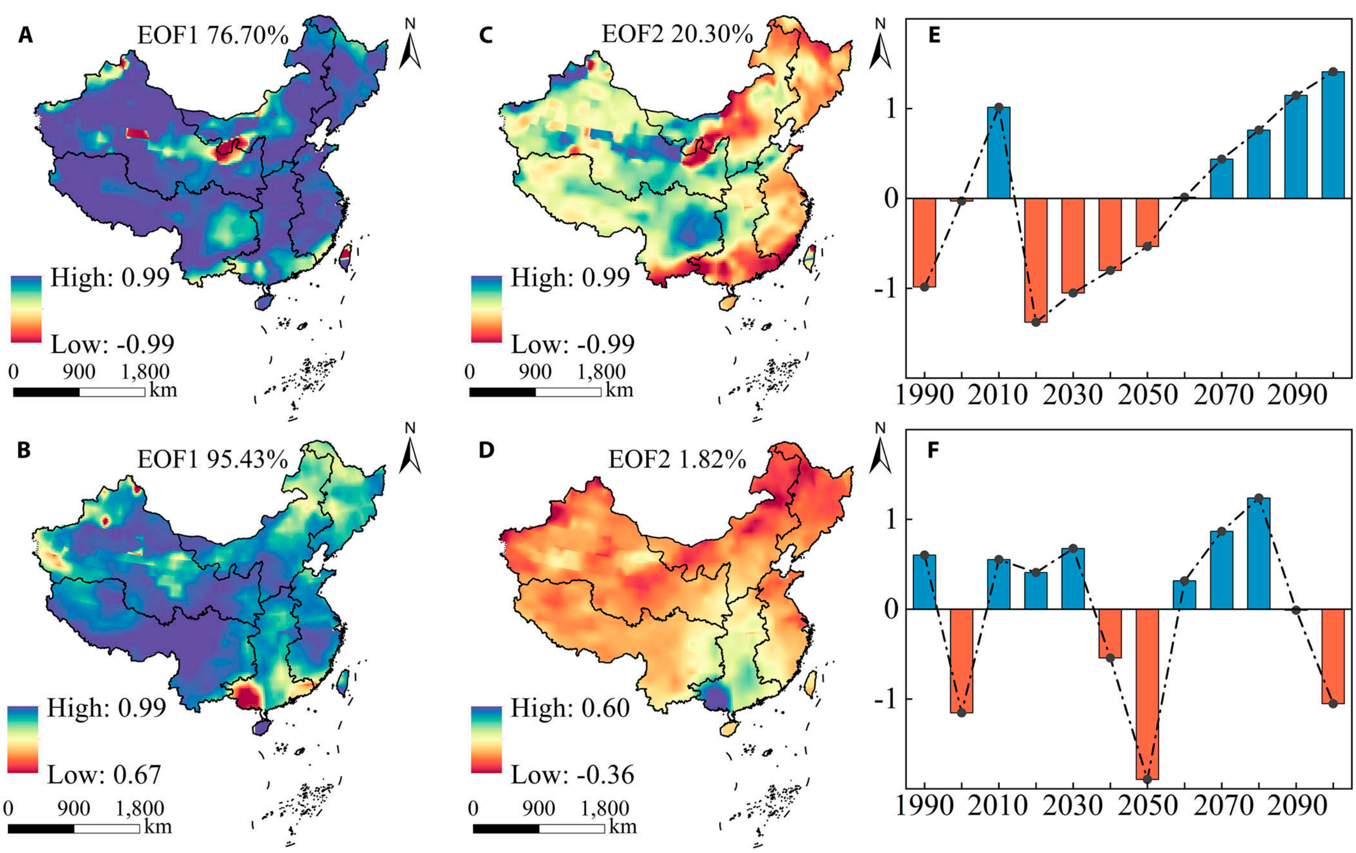

Fig. 10. Spatial distribution and time coefficients of the principal modes of GPP in China for 1981 to 2010 (A, C, and E) and 2011 to 2100 (B, D, and F) under SSP5-8.5. China map: GS (2024) 0650 (Ministry of Natural Resources).

precipitation, with event duration consistently showing the strongest effect. SEM results (1981 to 2100) indicate a stable mechanism linking extreme events to GPP changes. While the historical period reflects a composite effect of multiple factors, the future is dominated by prolonged high-temperature events, likely due to cumulative exposure exceeding vegetation tolerance thresholds. This highlights ecosystem sensitivity to long-term climate stress, with event duration being the most critical driver of GPP changes.

Uncertainty

The data quality of the GCMs selected in this study has been widely verified, and the resolution of downscaled products has been improved. In the future, the reliability of the data should be further improved by improving the downscaling method through the fusion and comparison of data from multiple sources. This study mainly characterizes the impact of climate factors on the GPP of terrestrial ecosystems, without fully considering the role of human activities; however, other extreme climate events and human impacts (land-use change, irrigation, ecological restoration, urbanization, etc.) can also affect vegetation productivity. For instance, regions with substantial ecological restoration or afforestation may exhibit GPP increases regardless of climatic extremes, meaning that climate-only attribution could overestimate or misrepresent the role of climate in such areas. Future research should include more extreme climate indices (such as the extreme drought index), soil data (soil type, texture, moisture content, irrigation, etc.), vegetation physiological parameters (such as leaf area index), and human activity indices (population density, etc.).

Conclusion

This study evaluated the spatiotemporal patterns and temporal trends of GPP across China (1981 to 2100) using extreme climate indices and GPP data, focusing on the impact of extreme precipitation–high-temperature events. Key findings are as follows: (a) GPP increases overall, with growth rates rising from SSP1-2.6 to SSP5-8.5. Substantial differences in GPP emerge after 2040, with growth accelerating after 2031 in SSP1-2.6, while high-emission scenarios see delayed acceleration. (b) GPP exhibits a pronounced south–north gradient—highest in the south and lowest in the north—with most regions showing upward trends. National GPP exhibits synchronized growth and decline across regions. (c) The GPP center of gravity shifts westward and northward, with the largest movement under SSP5-8.5. Future shifts will move GPP from densely vegetated eastern and southern regions to sparser western and northern areas, improving overall ecological conditions. (d) Under SSP5-8.5, extremely high temperature (especially duration/total days) becomes the greater factor affecting GPP, while other scenarios are primarily influenced by extreme precipitation (duration/total days, intensity). As emissions rise, the impact of extreme precipitation and high temperature on GPP shifts from positive to negative, with duration/total days having the strongest effect. Negative effects are persistent in NEC, while SC, NWC, NC, and SWC transition from positive to negative under high emissions, and EAC shows fluctuating positive and negative impacts. The rising frequency, intensity, and duration of extreme events under climate change pose severe threats to terrestrial carbon sinks and carbon cycle stability. It is recommended that China enforce ecological protection red lines and establish an efficient ecological carbon sink management system.

Acknowledgments

The authors would like to thank the anonymous reviewers and editors for their invaluable comments to improve this paper.
Funding: This work was supported by the Open Fund of South China Institute of Environmental Sciences, Ministry of Ecology and Environmental and State Environmental Protection Key Laboratory of Urban Ecological Simulation and Protection (UEESP-202505), the Key Laboratory of Remote Sensing Application and Innovation (LRSAI-2025012), and the National Natural Science Foundation of China (41601184).
Author contributions: Z.S. and Y.L.: Conceptualization, methodology, software, visualization, and writing—original draft preparation. H.Y. and Y.L.: Conceptualization, validation, supervision, funding acquisition, writing—original draft preparation, manuscript reviewing, and editing. L.L.: Visualization. J.S. and L.J.: Writing—reviewing and editing.
Competing interests: The authors declare that they have no competing interests.

Data Availability

Data will be made available on request.

Supplementary Materials

Figs. S1 to S7
Tables S1 to S3

References

1. Wei N, Xia J. Robust projections of increasing land carbon storage in boreal and temperate forests under future climate change scenarios. *One Earth*. 2024;7(1):88–99.
2. Ruehr S, Keenan TF, Williams C, Zhou Y, Lu X, Bastos A, Canadell JG, Prentice IC, Stich S, Terrer C. Evidence and attribution of the enhanced land carbon sink. *Nat Rev Earth Environ*. 2023;4(8):518–534.
3. Gao YH, Zhu D, Wang Z, Lin Z, Zhang Y, Wang K. Projected increasing negative impact of extreme events on gross primary productivity during the 21st century in CMIP6 models. *Earth Future*. 2024;12(11):Article e2024EF004798.
4. Higgins SI, Conradi T, Muhoko E. Shifts in vegetation activity of terrestrial ecosystems attributable to climate trends. *Nat Geosci*. 2023;16(2):147–153.
5. Tang XL, Zhao X, Bai YF, Tang Z, Wang W, Zhao Y, Wan H, Xie Z, Shi X, Wu B, et al. Carbon pools in China's terrestrial ecosystems: New estimates based on an intensive field survey. *Proc Natl Acad Sci USA*. 2018;115(16):4021–4026.
6. Gampe D, Zscheischler J, Reichstein M, O'Sullivan M, Smith WK, Sitch S, Buermann W. Increasing impact of warm droughts on northern ecosystem productivity over recent decades. *Nat Clim Chang*. 2021;11(9):772–779.
7. Zhang YC, Hong SB, Liu D, Piao S. Susceptibility of vegetation low-growth to climate extremes on Tibetan plateau. *Agric For Meteorol*. 2023;331:Article 109323.
8. Piao SL, Zhang XP, Chen AP, Liu Q, Lian X, Wang X, Peng S, Wu X. The impacts of climate extremes on the terrestrial carbon cycle: A review. *Sci China-Earth Sci*. 2019;62(10):1551–1563.

9. Lian X, Peñuelas J, Ryu Y, Piao S, Keenan TF, Fang J, Yu K, Chen A, Zhang Y, Gentine P. Diminishing carryover benefits of earlier spring vegetation growth. *Nat Ecol Evol*. 2024;8(2):218–228.
10. Alkama R, Forzieri G, Duveiller G, Grassi G, Liang S, Cescatti A. Vegetation-based climate mitigation in a warmer and greener world. *Nat Commun*. 2022;13(1):606.
11. Van Der Woude AM, Peters W, Joetzjer E, Lafont S, Koren G, Ciais P, Ramonet M, Bastos A, Botia S, Stich S, et al. Temperature extremes of 2022 reduced carbon uptake by forests in Europe. *Nat Commun*. 2023;14(1):6218.
12. Jiang C, Ryu Y. Multi-scale evaluation of global gross primary productivity and evapotranspiration products derived from breathing earth system simulator (BESS). *Remote Sens Environ*. 2016;186:528–547.
13. Chen YZ, Feng XM, Tian HQ, Wu X, Gao Z, Feng Y, Piao S, Lv N, Pan N, Fu B. Accelerated increase in vegetation carbon sequestration in China after 2010: A turning point resulting from climate and human interaction. *Glob Change Biol*. 2021;27(22):5848–5864.
14. Zhou H, Yue X, Wang B, Tian C, Lu X, Zhu J, Cao Y. Distinguishing the main climatic drivers to the variability of gross primary productivity at global FLUXNET sites. *Environ Res Lett*. 2023;18(12):124007.
15. Dang CY, Shao ZF, Fu P, Zhuang Q, Xu X, Qian J. Causal inference reveals the dominant role of interannual variability of carbon sinks in complicated environmental-terrestrial ecosystems. *Remote Sens Environ*. 2024;311:114300.
16. Li C, Sun G, Cohen E, Zhang Y, Xiao J, McNulty SG, Meentemeyer RK. Modeling the impacts of urbanization on watershed-scale gross primary productivity and tradeoffs with water yield across the conterminous United States. *J Hydrol*. 2020;583:124581.
17. Chen R, Li HY, Wang XJ, Gou X, Yang M, Wan G. Surface air temperature changes over the Tibetan plateau: Historical evaluation and future projection based on CMIP6 models. *Geosci Front*. 2022;13(6):101452.
18. Bjarke N, Livneh B, Barsugli J. Storylines for global hydrologic drought within CMIP6. *Earth Future*. 2024;12(6):Article e2023EF004117.
19. Zhang XY, Zhou Y, He W, Ju W, Liu Y, Bi W, Cheng N, Wei X. Land cover change instead of solar radiation change dominates the forest GPP increase during the recent phase of the shelterbelt program for Pearl River. *Ecol Indic*. 2022;136:108664.
20. Wild B, Teubner I, Moesinger L, Zotta R-M, Forkel M, van der Schalie R, Sitch S, Dorigo W. VODCA2GPP—A new, global, long-term (1988–2020) gross primary production dataset from microwave remote sensing. *Earth Syst Sci Data*, 2022, 14(3): 1063-85.
21. Zha JL, Shen C, Wu J, Zhao D, Fan W, Jiang H, Zhao T. Evaluation and projection of changes in daily maximum wind speed over China based on CMIP6. *J Clim*. 2023;36(5):1503–1520.
22. Latombe G, Burke A, Vrac M, Levavasseur G, Dumas C, Kageyama M, Ramstein G. Comparison of spatial downscaling methods of general circulation model results to study climate variability during the last glacial maximum. *Geosci Model Dev*. 2018;11(7):2563–2579.
23. Prodhan FA, Zhang J, Pangali Sharma TP, Nanzad L, Zhang D, Seka AM, Ahmed N, Hasan SS, Hoque MZ, Mohana HP. Projection of future drought and its impact on simulated crop yield over South Asia using ensemble machine learning approach. *Sci Total Environ*. 2022;807:151029.
24. Qiu BW, Yan XF, Chen CC, Tang Z, Wu W, Xu W, Zhao Z, Yan C, Berry J, Huang W, et al. The impact of indicator selection on assessment of global greening. *GISci Remote Sens*. 2021;58(3):372–385.
25. Maher N, Milinski S, Ludwig R. Large ensemble climate model simulations: Introduction, overview, and future prospects for utilising multiple types of large ensemble. *Earth Syst Dynam*. 2021;12(2):401–418.
26. Kotz M, Lange S, Wenz L, Levermann A. Constraining the pattern and magnitude of projected extreme precipitation change in a multimodel ensemble. *J Clim*. 2024;37(1):97–111.
27. Long D, Pan Y, Zhou J, Chen Y, Hou X, Hong Y, Scanlon BR, Longuevergne L. Global analysis of spatiotemporal variability in merged total water storage changes using multiple GRACE products and global hydrological models. *Remote Sens Environ*. 2017;192:198–216.
28. Lu D, Wang ZP, Su KC, Zhou Y, Li X, Lin A. Understanding the impact of cultivated land-use changes on China's grain production potential and policy implications: A perspective of non-agriculturalization, non-grainization, and marginalization. *J Clean Prod*. 2024;436:140647.
29. Zhang Q, Kong DD, Singh VP, Shi P. Response of vegetation to different time-scales drought across China: Spatiotemporal patterns, causes and implications. *Glob Planet Change*. 2017;152:1–11.
30. Gu ZP, Chen XW, Ruan WF, Zheng M, Gen K, Li X, Deng H, Chen Y, Liu M. Quantifying the direct and indirect effects of terrain, climate and human activity on the spatial pattern of kNDVI-based vegetation growth: A case study from the Minjiang River basin, Southeast China. *Ecol Inform*. 2024;80:102493.
31. Coppola E, Nogherotto R, Ciarlo' JM, Giorgi F, van Meijgaard E, Kadygrov N, Iles C, Corre L, Sandstad M, Somot S, et al. Assessment of the European climate projections as simulated by the large EURO-CORDEX regional and global climate model ensemble. *J Geophys Res-Atmos*. 2021;126(4): Article e2019JD032356.
32. Wang PY, Tang JP, Sun XG, Wang S, Wu J, Dong X, Fang J. Heat waves in China: Definitions, leading patterns, and connections to large-scale atmospheric circulation and SSTs. *J Geophys Res-Atmos*. 2017;122(20):10679–10699.
33. Yang L, Shen FX, Zhang L, Cai Y, Yi F, Zhou C. Quantifying influences of natural and anthropogenic factors on vegetation changes using structural equation modeling: A case study in Jiangsu Province, China. *J Clean Prod*. 2021;280:124330.
34. Su Z, Liang Y, Liu L. Confronting the dual climate challenge: A spatiotemporal assessment of extreme precipitation-high temperature events in China, 1981–2100. *Int J Environ Sci Technol*. 2025;22:15815–15830.
35. Shi SY, Yu JJ, Wang F, Wang P, Zhang Y, Jin K. Quantitative contributions of climate change and human activities to vegetation changes over multiple time scales on the loess plateau. *Sci Total Environ*. 2021;755:142419.
36. Babst F, Bouriaud O, Poulter B, Trouet V, Girardin MP, Frank DC. Twentieth century redistribution in climatic drivers of global tree growth. *Sci Adv*. 2019;5(1):Article eaat4313.
37. Zeng X, Hu ZM, Chen AP, Yuan W, Hou G, Han D, Liang M, di K, Cao R, Luo D. The global decline in the sensitivity of vegetation productivity to precipitation from 2001 to 2018. *Glob Change Biol*. 2022;28(22):6823–6833.

38. Chen SL, Huang YF, Wang GQ. Response of vegetation carbon uptake to snow-induced phenological and physiological changes across temperate China. *Sci Total Environ*. 2019;692:188–200.
39. Zhang T, Quan WJ, Tian JY, Li J, Feng P. Spatial and temporal variations of ecosystem water use efficiency and its response to soil moisture drought in a water-limited watershed of northern China. *J Environ Manag*. 2024;355:120251.
40. Liu YD, Zhang TY, Yuan LH, Zimini Y, Zhou R, Lin Z, Zheng C, Wen Z. Interannual asymmetric transitions of gross primary productivity in the grasslands of northern China. *Ecol Indic*. 2024;167:112631.
41. He W, Ju WM, Jiang F, Parazoo N, Gentine P, Wu X, Zhang C, Zhu J, Viovy N, Jain AK, et al. Peak growing season patterns and climate extremes-driven responses of gross primary production estimated by satellite and process based models over North America. *Agric For Meteorol*. 2021;298:108292.
42. Wang TH, Wang XF, Zhang Q, Zhang S, Tan J, Zhang Y, Ren Z, Yang Y, Che T. Effects of extreme temperature events on carbon fluxes in different ecosystems in the Heihe River Basin, China. *Agric For Meteorol*. 2025;362:110380.
43. Ji YY, Zeng SD, Liu X, Xia J. Mutual inhibition effects of elevated CO_2 and climate change on global forest GPP. *Environ Res*. 2024;252:119145.
44. Chang XQ, Xing YQ, Wang JQ, Yang H, Gong W. Effects of land use and cover change (LUCC) on terrestrial carbon stocks in China between 2000 and 2018. *Resour Conserv Recycl*. 2022;182:106333.
45. Xie SD, Mo XG, Hu S, Liu S. Contributions of climate change, elevated atmospheric CO_2 and human activities to ET and GPP trends in the three-north region of China. *Agric For Meteorol*. 2020;295:108183.
46. Keenan TF, Gray J, Friedl MA, Toomey M, Bohrer G, Hollinger DY, Munger JW, O'Keefe J, Schmid HP, Wing IS, et al. Net carbon uptake has increased through warming-induced changes in temperate forest phenology. *Nat Clim Chang*. 2014;4(7):598–604.
47. Lann T, Bao H, Lan HX, Zheng H, Yan C, Peng J. Hydro-mechanical effects of vegetation on slope stability: A review. *Sci Total Environ*. 2024;926:171691.
48. Nielsen UN, Ball BA. Impacts of altered precipitation regimes on soil communities and biogeochemistry in arid and semi-arid ecosystems. *Glob Change Biol*. 2015;21(4):1407–1421.
49. Jiang JL, Liu YM, Mao JY, Wu G. Extreme heatwave over eastern China in summer 2022: The role of three oceans and local soil moisture feedback. *Environ Res Lett*. 2023;18(4):044025.
50. Miao LJ, Ju L, Sun S, Agathokleous E, Wang Q, Zhu Z, Liu R, Zou Y, Lu Y, Liu Q. Unveiling the dynamics of sequential extreme precipitation-heatwave compounds in China. *NPJ Clim Atmos Sci*. 2024;7(1):67.

Ecosystem Health and Sustainability
A SCIENCE PARTNER JOURNAL

Extreme Precipitation and High-Temperature Impacts on Terrestrial Gross Primary Productivity across China, 1981 to 2100

Zichong Su, Huizhu Yang, Youjia Liang, Lijun Liu, Jia Sun, and Liangcun Jiang

Citation: Su Z, Yang H, Liang Y, Liu L, Sun J, Jiang L. Extreme Precipitation and High-Temperature Impacts on Terrestrial Gross Primary Productivity across China, 1981 to 2100. *Ecosyst Health Sustain*. 2025;**11**:0462. DOI: 10.34133/ehs.0462

The interplay of extreme precipitation and high temperature markedly diminishes the carbon sink capacity of China's terrestrial ecosystems. Although the spatiotemporal evolution characteristics of these extreme events have been initially identified, their impacts on gross primary production (GPP) remain inadequately quantified. With the multisource data (1981 to 2100) of 4 shared socioeconomic pathways (SSPs), the Mann–Kendall test, empirical orthogonal function, and center of gravity shift models were used to identify the spatiotemporal evolution of GPP, and the structural equation model was used to elucidate the pathways and contributions of extreme events to GPP changes. GPP increased nationwide (0.02 to 0.07 kg C m#2 a#1 decade#1, P < 0.05), with growth varying by scenario and there is regional heterogeneity; the first principal mode of GPP was positive in most areas (59.55% to 100%), with the same increasing and decreasing characteristics; the spatial centroid of GPP exhibited a shift from the east and south toward the west and north, accompanied by marked ecosystem greening; extremely high temperature exerted the most -substantial negative influence on GPP under SSP5-8.5 (standardized path coefficients: #0.580), whereas extreme precipitation duration in SSPs 1-2.6 and 3-7.0, and intensity in SSP2-4.5. The total effect of extreme events on GPP change shifts from a positive to a negative effect (0.966 # #0.655, #167.81%) with increasing carbon emissions. Negative effects are concentrated in Northeast China, East China shows alternating positive and negative effects, and the other regions shift from positive to negative effects. This study emphasizes the importance of differentiated climate change adaptation capacity building.
Image

View the article online
https://spj.science.org/doi/10.34133/ehs.0462

Ecosystem Health and Sustainability (ISSN 2332-8878) is published by the American Association for the Advancement of Science. 1200 New York Avenue NW, Washington, DC 20005.